Journal of Energy Chemistry 86 (2023) 437–446

Contents lists available at ScienceDirect

Journal of Energy Chemistry

journal homepage: www.elsevier.com/locate/jechem

http://www.journals.elsevier.com/journal-of-energy-chemistry/

Hydrogen production at intermediate temperatures with proton conducting ceramic cells: Electrocatalytic activity, durability and energy efficiency

Haoyu Zheng [a,b,*], Feng Han [a], Noriko Sata [a], Rémi Costa [a,*]

[a] Institute of Engineering Thermodynamics, German Aerospace Center (DLR), Stuttgart 70569, Germany
[b] Institute for Building Energetics, Thermotechnology and Energy Storage (IGTE), University of Stuttgart, Stuttgart 70569, Germany

ARTICLE INFO

Article history:
Received 25 May 2023
Revised 21 July 2023
Accepted 22 July 2023
Available online 11 August 2023

Keywords:
Steam electrolysis
Hydrogen production
Proton conducting ceramics
Intermediate temperature
Energy efficiency

ABSTRACT

Proton conducting ceramic cells (PCCs) are an attractive emerging technology operating in the intermediate temperature range of 500 to 700 °C. In this work, we evaluate the production of hydrogen at intermediate temperatures by proton conducting ceramic cell electrolysis (PCCEL). We demonstrate a high-performance steam electrolysis owing to a composite positrode based on $BaGd_{0.8}La_{0.2}Co_2O_{6-\delta}$ (BGLC1082) and $BaZr_{0.5}Ce_{0.4}Y_{0.1}O_{3-\delta}$ (BZCY541). The high reliability of PCCEL is demonstrated for 1680 h at a current density as high as –0.8 A cm^{-2} close to the thermoneutral cell voltage at 600 °C. The electrolysis cell showed a specific energy consumption ranging from 54 to 66 kW h kg^{-1} that is comparable to state-of-the-art low temperature electrolysis technologies, while showing hydrogen production rates systematically higher than commercial solid oxide ceramic cells (SOCs). Compared to SOCs, the results verified the higher performances of PCCs at the relevant operating temperatures, due to the lower activation energy for proton transfer comparing with oxygen ion conduction. However, because of the p-type electronic conduction in protonic ceramics, the energy conversion rate of PCCs is relatively lower in steam electrolysis. The faradaic efficiency of the PCC in electrolysis mode can be increased at lower operating temperatures and in endothermic conditions, making PCCEL a technology of choice to valorize high temperature waste heat from industrial processes into hydrogen. To increase the faradaic efficiency by optimizing the materials, the cell design, or the operating strategy is a key challenge to address for future developments of PCCEL in order to achieve even more superior techno-economic merits.

1. Introduction

The global hydrogen demand reached 94 million tons (Mt) in 2021 representing 2.5% of the global energy consumption [1]. The current hydrogen production is mainly based on steam methane reforming and coal gasification [2], which is responsible for more than 900 Mt of CO_2 emissions annually [3]. Hydrogen is commonly used in refineries for the petrochemistry and chemical industry, and a growing demand of hydrogen is expected from the hard-to-abate sector such as the aviation, heavy industry, shipping, heavy-duty transportation, or district heating [1]. Hydrogen production by water electrolysis powered by renewable resources has low CO_2 emission and is of utmost importance for the decarbonization of the energy and transportation sectors [4]. Water electrolysis is an endothermic process. It is especially efficient at high temperatures when steam is used as the feedstock, as a significant portion of the energy required for the water splitting is supplied in the form of heat [5]. High temperature steam electrolysis based on solid oxide electrolysis (SOEL) performed typically at temperatures above 800 °C is proven to be the most efficient technology compared to the low temperature ones such as alkaline electrolysis (AEL), polymer exchange membrane electrolysis (PEMEL) and anion exchange membrane electrolysis (AEMEL) [5].

SOEL is usually performed under isothermal conditions, that is at a cell voltage close or slightly higher than the thermoneutral voltage (V_{TN}, ~1.28 V). At V_{TN} and under ideal adiabatic conditions,

* Corresponding authors.
E-mail addresses: zhenghaoyu01@gmail.com (H. Zheng), remi.costa@dlr.de (R. Costa).

https://doi.org/10.1016/j.jechem.2023.07.030

the electrical energy conversion in the cell is 100%. In reality, the voltage is maintained slightly above V_{TN} to enable a slight heat generation and to balance the heat losses to the environment, keeping the cell or the stack in isothermal conditions. SOEL operation in isothermal condition is favoured by the supply of superheated steam at a temperature very close to the nominal stack operating temperature in order to avoid critical thermal gradient along the gas channels. In SOEL, the water splitting occurs at the fuel electrode (negatrode) of the solid oxide ceramic cells (SOCs) which is generally made of a cermet of nickel mixed with an oxygen ion conducting ceramic, for example, yttria-stabilized zirconia (YSZ) or gadolinia-doped ceria (GDC) [6,7]. The supplied steam is mixed with a fraction of 5% to 10% hydrogen in order to maintain constant reducing conditions and to avoid the oxidation of the nickel in the cermet electrode. The electrolysis process yields typically a 70%–80% hydrogen-rich stream at the stack outlet, with unconverted steam as the balance. This large fraction of steam in the outlet stream together with the high temperature poses the significant challenge of the recirculation and heat recovery in terms of materials selection, design, and durability of the blower and the heat exchangers, respectively [8–10]. Moreover, the remaining steam must be removed in most of the use cases of the produced hydrogen.

High temperature electrolysis in the intermediate range that is typically around 600 °C is less demanding for the structural materials and offers, therefore, significant perspectives for a superior longevity compared to SOEL [11,12]. Moreover, the intermediate operating temperature range is especially attractive for valorising the waste heat from industrial processes. The Carnot waste heat recovery potential for high temperature waste heat, i.e., at temperature above 300 °C, exceeds 150 terawatt-hour (TW h) per year in the European industry alone with iron and steel and non-metallic minerals industries as major sources [13,14]. Proton conducting ceramic cells (PCCs) can be operated at intermediate temperatures (400–700 °C) in electrolysis (PCCEL) due to a lower activation energy for proton transfer compared to oxygen ion transfer in SOCs [15–17]. In PCCs, Y-doped $BaZrO_3$–$BaCeO_3$ solid solution materials, i.e., $BaZr_{1-x-y}Ce_xY_yO_{3-\delta}$ (BZCY), are state-of-the-art electrolytes . BZCY exhibits mixed ionic and electronic conductivity. The charge carriers in BZCY are electron holes, protons, and oxygen ions, and their respective prevalence is influenced by the precise materials composition itself, the operating temperature and the gas atmosphere [18]. Electron holes are formed in BZCY electrolyte materials upon oxygen incorporation, which is given by

$$\frac{1}{2}O_2 + V_O^{\cdot\cdot} \rightleftarrows O_O^x + 2h^{\cdot} \quad (1)$$

The reaction is endothermal, meaning that the formation of electron holes is enhanced at higher temperatures. The prevalence of electron holes causes electronic leakage through the electrolyte layer, which leads to a low faradaic efficiency and, thus, to a low electrical efficiency. The electronic leakage is minimal in fuel cell operation [19,20]. In electrolysis mode, however, the operating conditions favor p-type conduction in the electrolyte, and the faradaic efficiency shows a strong dependency on the oxygen partial pressure (pO_2), steam partial pressure (pH_2O), working temperature and the anodic overpotential at the oxygen electrode (positrode). To date, the observed faradaic efficiency values exhibit a wide range spanning from ~30% to ~85% under thermoneutral conditions (Table S1). Furthermore, operation in the intermediate temperature range is concomitant with lower reaction rates in relation with the oxygen reduction reaction (ORR) and the oxygen evolution reaction (OER) at the oxygen electrode (positrode) [21]. Therefore, positrode materials with high electrocatalytic activities are crucial for the development of high-performance PCC technology [22]. Double perovskite structure materials based on $Ba_{1-x}Gd_{0.8}La_{0.2+x}Co_2O_{6-\delta}$ (x = 0–0.5) (BGLC) with water uptake properties have been thoroughly investigated [23,24]. The electrochemical behavior of $Ba_{0.5}Gd_{0.8}La_{0.7}Co_2O_{6-\delta}$ (BGLC587) mixed with BZCY541 into composite positrode has been investigated as a function of the gas atmosphere, the temperature, and the applied electrical bias. The effect of these operating conditions on the current leakage and faradaic efficiency in electrolysis mode was extensively discussed [25]. It was demonstrated by Vøllestad et al. that BGLC with x = 0 (BGLC1082) possesses the largest concentration of oxygen vacancies and shows the highest electrical conductivity in a useful pO_2 and temperature range, that is between 1 and 10^{-5} atm and between room temperature and 800 °C, respectively [26].

Here, we evaluated the production of hydrogen at intermediate temperatures by steam electrolysis with PCCs in terms of performance, durability and figure of merits compared to other electrolysis technologies. Since the formation of protonic defect ($OH^{\bullet}$) by hydration reaction consumes oxygen vacancies, the composition BGLC1082 is likely to possess the highest electrocatalytic activity among the BGLC compounds (with $x \geq 0.1$). We manufactured a proton conducting ceramic cell with a composite positrode of BGLC1082–BZCY541. High performance and durable PCCEL at a current density as high as –0.8 A cm^{-2} at thermoneutral voltages over 1680 h operation was achieved. Furthermore, steam electrolysis at intermediate temperatures with PCCs was systematically compared with the state-of-the-art SOCs for hydrogen production. The PCC exhibited systemically higher hydrogen production rate. However, due to the existence of current leakage across the electrolyte, PCCs demonstrated a lower energy conversion efficiency compared to SOCs. The endothermic operating regime in combination with waste heat recovery is highlighted as the most promising operating strategy for PCCEL to achieve high energy efficiency.

2. Experimental

2.1. Materials preparation

$BaGd_{0.8}La_{0.2}Co_2O_{6-\delta}$ (BGLC1082) and $BaZr_{0.5}Ce_{0.4}Y_{0.1}O_{3-\delta}$ (BZCY541) commercial powders (Marion Technologies, Verniole, France) were used in this study. The BZCY541 raw powder was annealed in air at 1400 °C for 5 h before using. The BGLC1082 raw powder was treated at 600 °C for 65 h with 30% steam/Air in order to investigate its stability in moist atmosphere.

2.2. Full cells fabrication

Proton conducting ceramic cells: negatrode supported proton conducing ceramic full cells were fabricated. NiO (Marion Technologies, Verniole, France), BZCY541 and starch (REMY FG P, BENEO GmbH, Germany) (weight ratio of 6:4:1) were mixed in 2-propanol by planetary ball milling for 3 h, and the obtained mixture was dried in an oven at 65 °C. 1 g of the mixture was pressed in a 20 mm diameter die at 60 MPa uniaxial. The green pellet was pre-sintered at 1150 °C for 2 h to enhance the mechanical strength for the next processing steps. BZCY541 electrolyte was deposited on NiO-BZCY substrate by drop-coating. The suspension was prepared by mixing BZCY541 raw powder, ethanol, polyvinyl butyral, polyethylene glycol and triethanolamine on a roll-miller for 12 h. When a homogeneous suspension was formed, 200 μL of the electrolyte suspension was dropped on the surface of the NiO-BZCY541 substrate. After drying, the assembly was co-sintered in air at 1450 °C for 5 h, resulting in the formation of half cells. During sintering, the sample was covered by the raw powder to prevent Ba evaporation. For the positrode, BGLC1082 and BZCY541 with the weight ratio of 6:4 were mixed in ethanol, ball-milled for 5 h with 400 r min^{-1} in a planetary ball mill, and finally dried at 60 °C. A

fraction of the obtained powder mixture was annealed in air at 1000 °C for 2 h to check the chemical compatibility of the two components while the rest was blended with a ink vehicle (6 wt.% ethyl cellulose in terpineol) in a three-roll mill to form a homogenous ink. This ink was subsequently screen printed onto the surface of the BZCY541 electrolyte of the half cells and calcined at 900 °C for 2 h. A Pt paste (Heraeus GmbH, Germany) was painted on the positrode and fired at 700 °C for 1 h as a current contacting layer. The active area of the full cell was 0.5 cm^2.

Solid oxide ceramic cells: commercial SOCs (ASC-400B) from Elcogen AS (Estonia) were used in this study. The SOCs consist of a NiO-YSZ substrate (400 ± 30 μm) with a diameter of 20 mm, a NiO-YSZ negatrode layer (~10 μm), a YSZ electrolyte (3 ± 1 μm), a GDC barrier layer (2 ± 1 μm) and an LSC ($La_{0.6}Sr_{0.4}CoO_{3-\delta}$) positrode (15 ± 5 μm). The active area of the SOC full cell is 0.79 cm^2. A Pt paste was brushed on the top of the LSC positrode and calcined at 700 °C for 1 h to keep the consistency of the experiments with PCCs measurements.

2.3. Characterization

X-ray diffraction (XRD) with a D8 Discover GADDS and equipped with a VÅNTEC-2000 area detector was used to analyze the ceramic powders (Bruker AXS, Germany). The diffraction pattern was recorded using a tuned monochromatic and collimated Cu K_α radiation source in Bragg-Brentano geometry. The ICDD database was used to identify crystal phases. Microstructures of the different functional layers and elemental mapping were observed using a Zeiss Crossbeam 350 scanning electron microscope (SEM, Carl Zeiss AG, Germany) with the energy dispersive X-ray spectroscopy (EDS) detector of Oxford ULTIM MAX 100 mm^2.

2.4. Electrochemical measurement

The as-prepared proton conducting ceramic cells with BGLC1082–BZCY541 positrode were investigated in steam electrolysis operation using an electrochemical test system. The system comprises the ProboStat base unit (NORECS AS, Norway) as the cell housing, humidifier (HumiStat, NORECS AS, Norway) for water evaporation, mass flow controllers (Vögtlin Instruments GmbH, Switzerland) and a mass spectrometer (EISense, V&F Analyse und Messtechnik GmbH) for outlet gas analysis. For the test, Pt meshes were attached on both positrode and negatrode as the current collectors, and each Pt mech was connected with two Pt wires. The 2-electrodes 4-wires method was used for all the electrochemical measurements. A ceramic sealant (Ceramabond 552, AREMCO, USA) together with a glass paste (617, AREMCO, USA) were used to ensure gas-tight sealing between the two electrodes. After curing the sealants, the cells were heated up to 700 °C by 3 °C min^{-1} with 5%H_2/N_2 supplied to the negatrode and air supplied to the positrode. After 12 h reduction, the gas feed to the negatrode was switched to pure H_2 until the open circuit voltage (OCV) became stable. The electrochemical performance of the PCCs was tested in fuel cell mode first with wet air supplied to the positrode side and wet H_2 to the negatrode side. Polarization curves were recorded at the voltages from OCV to 0.3 V with a scanning rate of 0.005 V s^{-1}.

In steam electrolysis operation, polarization curves were recorded from OCV to 1.5 V at the operation temperatures from 500 to 700 °C with 30%H_2O/air was supplied to the positrode and wet (~3% H_2O) 20%H_2/N_2 was supplied to the negatrode. A long-term stability test was performed in galvanostatic mode, lasting for a total of 1680 h. The SOCs were tested in the same apparatus following a similar protocol. Air was supplied to the positrode, and 30%H_2O–20%H_2–50%N_2 was supplied to the negatrode at a flow rate of 50 sccm on both electrode sides. Polarization curves and electrochemical impedance spectra (EIS) at OCV were recorded in the temperature range of 550–700 °C. Electrochemical impedance measurements were performed in the frequency range from 100 kHz to 0.1 Hz at the amplitude of 20 mV. Equivalent circuit model (ECM) fitting was carried out using ZView®. The faradaic efficiency (η_{FE}) of PCCs for steam electrolysis was calculated by analyzing the deviation between theoretical hydrogen production rate with the actual hydrogen production rate.

3. Results and discussion

3.1. PCCEL at intermediate temperatures

In PCCEL, the water splitting process occurs at the positrode, and the generated mobile protons, which are introduced by the hydration process ($V_O^{\cdot\cdot} + O_O^x + H_2O \rightleftarrows 2OH_O^{\cdot}$) in a wet atmosphere, transfer from the positrode to the negatrode. On the negative electrode, the protons are reduced to hydrogen ($2H^+ + 2e^- \rightarrow H_2$), while the oxygen evolution process ($2O^{2-} \rightarrow O_2 + 4e^-$) takes place on the positrode side to produce the by-product of oxygen, as shown in Fig. 1(a). We have used a negatrode supported planar PCC with the composite positrode of BGLC1082–BZCY541 for hydrogen production.

By the XRD analysis, the BGLC1082 powder displayed a layered perovskite structure in tetragonal P4/mmm space group (Fig. S1a) [24,27]. Recently, a water-induced surface modification phenomenon and performance enhancement was observed in double perovskite structure materials with cobalt on B-site [28–30]. The in-situ exsolved $BaCoO_{3-\delta}$ phase was shown to be the active site for rapid oxygen adsorption and dissociation process. In BGLC1082, the $BaCoO_{3-\delta}$ phase was detected by treating the raw power in 30% steam/air at 600 °C for 65 h (Fig. S1b). Exploring the mechanism of $BaCoO_{3-\delta}$ exsolution in the BGLC1082 goes beyond the scope of this study. Chemical compatibility between BGLC1082 and BZCY541 was confirmed by checking the phases of the mixture of BGLC1082–BZCY541 annealed in air at 1000 °C for 2 h. No secondary phase formation or decomposition was observed (Fig. S1a).

The PCC consists of a ~800 μm thick negatrode (Ni–BZCY541), a ~10 μm thick electrolyte (BZCY541) and the composite positrode (BGLC1082–BZCY541) of 30 μm in thickness (Fig. 1b). Current densities of −1.60, −1.23, −0.83, −0.51 and −0.27 A cm^{-2} were achieved at thermoneutral voltage (~1.28 V) and the operating temperatures of 700, 650, 600, 550 and 500 °C, respectively (Fig. 1c). The measured current density is 8 times higher than the previous research in a tubular cell with a similar positrode, in which the current density was limited to around −0.10 A cm^{-2} at ~1.28 V and 600 °C [24]. This is also higher than our previous work with BGLC587–BZCY541 composite positrode cells (−0.65 A cm^{-2} at 1.3 V and 600 °C) [25]. Furthermore, we demonstrated an excellent performance of the cell with peak power densities of 506, 667 and 833 mW cm^{-2}, respectively, at 600, 650 and 700 °C in fuel cell mode as well (more details see Note S1 and Fig. S2). The results confirmed that the BGLC1082–BZCY541 composite positrode exhibits remarkable electrocatalytic activity towards both the ORR and OER processes.

The measured (V_{OC}) and theoretical (V_T) open circuit voltages revealed increasing discrepancies upon temperature increase (Fig. 1c). For a better understanding of this phenomenon, electrochemical impedance spectra (EIS) measurements were performed at OCV (Fig. 1d). An equivalent circuit model (Fig. S4a) was used for the EIS data fitting. The ohmic resistance (R_Ω) is determined by the high frequency intercept with the real axis. Considering the mixed ionic and electronic transport properties of the BZCY541 electrolyte, R_Ω is the sum of ionic resistance ($R_{\Omega,i}$) and electronic resistance ($R_{\Omega,e}$). The ionic transference number (t_i) and the elec-

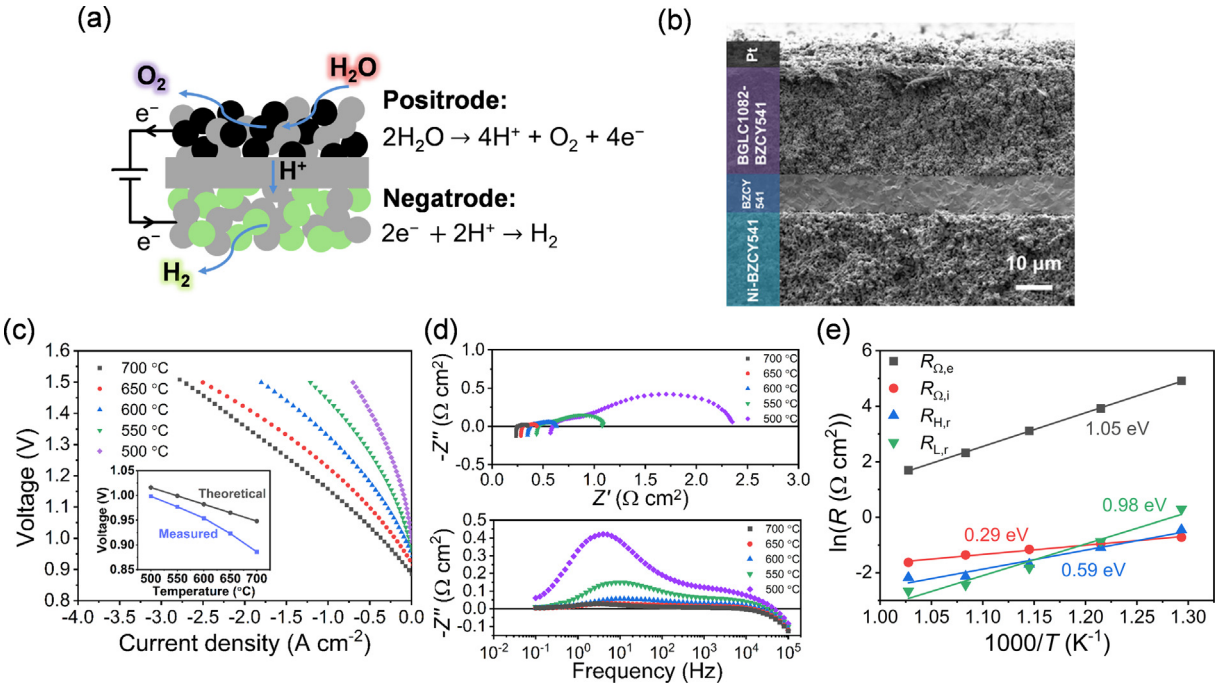

Fig. 1. (a) Schematic illustration of the PCCs for steam electrolysis. (b) SEM cross-section image of the as-prepared PCCs. (c) Polarization curves recorded in steam electrolysis mode with 30% steam/air supplied to the positrode and 20% H_2/N_2 to the negatrode (inside, the comparison between the measured open circuit voltages and the theoretical values); and the corresponding electrochemical impedance spectra recorded at OCV (d). (e) Arrhenius plot of the electronic resistance ($R_{\Omega,e}$), ionic resistance ($R_{\Omega,i}$), and corrected polarization resistance ($R_{H,r}$ and $R_{L,r}$).

tronic transference number (t_e) can be calculated (Fig. S5), accordingly [23,31,32]. The value of t_i decreased from 0.996 at 500 °C to 0.965 at 700 °C, indicating the increased electronic conductivity at higher temperatures. By neglecting the contact resistances, the conductivity of the electrolyte (σ_Ω) can be calculated using the following equation:

$$\lim_{\omega\to\infty}\{Z\} = R_\Omega + R_{contact} \approx \frac{L}{\sigma_\Omega}, \quad (2)$$

where L is the thickness of the electrolyte. Therefore, the ionic ($\sigma_{\Omega,i}$) and electronic ($\sigma_{\Omega,e}$) conductivities of the electrolyte can be determined (Fig. S6). Both $\sigma_{\Omega,i}$ and $\sigma_{\Omega,e}$ increased at elevated temperatures, with $\sigma_{\Omega,i}$ ranging from 0.002 to 0.006 S cm^{-1} between 500 and 700 °C, which is in good agreement with the previously reported BZCY541 conductivity values [33]. Besides, the $\sigma_{\Omega,e}$ is more than 2 orders of magnitude lower than $\sigma_{\Omega,i}$ at low temperatures. To quantify this electronic leakage based on the EIS results, we employed the method developed by Choi et al. [34],

$$I_{OC}(e^-) = -I_{OC}(H^+) = -\frac{-V_{OC}}{R_t}\left(1 - \frac{V_{OC}}{V_N}\right), \quad (3)$$

where $I_{OC}(e^-)$ and $I_{OC}(H^+)$ are the electronic and protonic current densities at open circuit voltages, and R_t is the total resistance at V_{OC}. The current leakage was estimated to be between 0.007 A cm^{-2} at 500 °C, and 0.163 A cm^{-2} at 700 °C, confirming the impact of the p-type electronic conduction through the electrolyte and an accelerated current leakage at higher temperatures.

The polarization resistance (R_P) is given by the intercepts between high and low frequencies with the real axis. In the Nyquist plot, the impedance curve shows a predominant low frequency arc (R_L) that is generally assigned to a surface related diffusion process and a high frequency arc (R_H) that is assigned to a charge transfer process. The real polarization resistance at high frequencies ($R_{H,r}$) and low frequencies ($R_{L,r}$) are obtained from the same equivalent circuit model fitting. Current leakage leads to discrepancies between apparent values and true polarization values, that is determined by considering the current leakage (as presented in Table S2). The activation energy (E_a) is calculated by using the corrected resistance values obtained from the fitting results. The calculated E_a of R_i is 0.29 eV, which is relatively low in comparison with the reported E_a values of proton migration through the bulk [35]. Besides, the E_a of $R_{H,r}$ and $R_{L,r}$ are 0.59 and 0.98 eV, respectively. For negatrode-supported PCCs, the polarization resistance is demonstrated mainly from the positrode [25,28], and the E_a of $R_{L,r}$ is quite close to the reported E_a of the oxygen surface exchange coefficient for ordered cobaltites [36,37]. The E_a of R_e shows the highest values of 1.05 eV.

3.2. Current leakage and faradaic efficiency in PCCEL

Under polarization, the conduction of electron holes through the BZCY electrolyte leads to the current leakage during electrolysis, resulting in a net reduction of the effective current for proton reduction at the negatrode (step 5 in Fig. 2a). Zhu et al. [19] reported that the flux of all charge carriers under high polarization current is dominated by the migration flux which is directly proportional to the conductivity of the electrolyte under the conditions at positrode side and thus, related to the transference number of the corresponding charge carriers, as at open circuit conditions.

The total current density, that is the applied current density, and the terminal voltages are summarized in Fig. 2(b). The faradaic efficiency was calculated by comparing the detected H_2 production rate with the theoretical values (Fig. 2c). The measurement was performed under galvanostatic mode at each measurement point for more than 30 min until the detected outlet gas composition was stable. At V_{TN}, the maximum faradaic efficiency reached 64% at 550 °C (Fig. 2c), which is competitive with previous reports as summarized in Table S1. At a given voltage, the faradaic efficiency decreased upon temperature increase. Moreover, the faradaic efficiency reduced dramatically with the increase of terminal voltage.

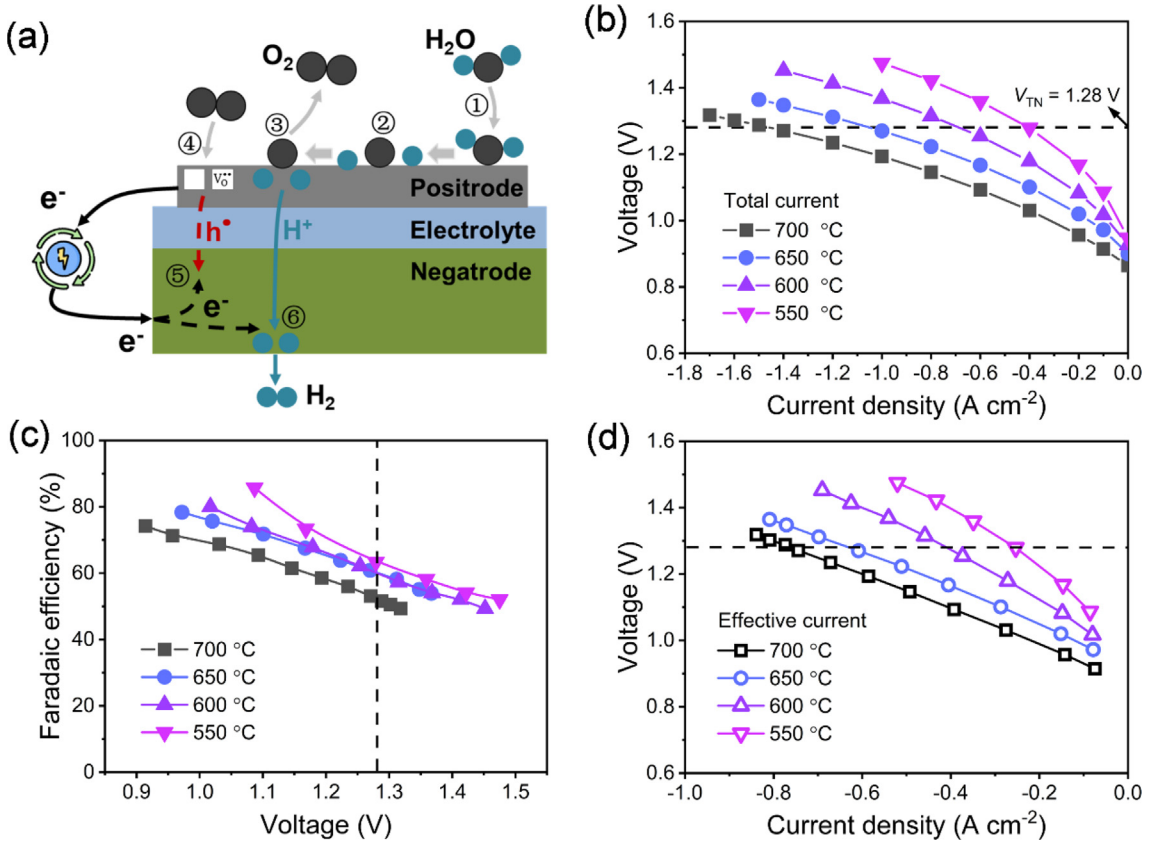

Fig. 2. Characterizations of PCCs with BGLC1082-BZCY541 composite positrode for steam electrolysis at different operating temperatures. (a) Schematic illustration of the PCCs for steam electrolysis accompanied with electronic current leakage (step 1: water adsorption, step 2: incorporation, step 3: oxygen release and proton transfer, step 4: oxygen incorporation, step 5: Null ⇌ $h^{\bullet} + e^-$, step 6: proton reduction [24]). (b) Apparent polarization curves. (c) The measured faradaic efficiency as a function of voltage. (d) Polarization curves corrected by the corresponding faradaic efficiency and plotted as a function of the effective current density.

Vøllestad et al. [24] demonstrated the relation between the concentration of electron holes and the potential E,

$$[h^{\cdot}] = K_{OX}[OH_O^{\cdot}]p_{H_2O}^{-\frac{1}{2}}p_{O_2}^{\frac{1}{4}} = K_{OX}\exp\left[\frac{F(E-E^0)}{RT}\right]. \quad (4)$$

Additionally, as reported by Duan et al. [12] the steam partial pressure (pH_2O) and oxygen partial pressure (pO_2) at the interface of electrolyte/positrode can be estimated using Fick's first law. The pH_2O at the interface is decreased during electrolysis operation at high current density, and the generation of oxygen increases the pO_2. Since higher pO_2 and lower pH_2O conditions promote the formation of electron holes, this leads to a negative feedback loop resulting in a more pronounced decrease of the faradaic efficiency at higher current density. Therefore, the effective current yielding net hydrogen production is reduced to −0.26, −0.41, −0.63 and −0.76 A cm^{-2} at 1.28 V and temperatures of 550, 600, 650 and 700 °C, respectively (Fig. 2d).

3.3. Long-term durability of PCCEL

The durability of electrolysis cells and stacks is a crucial factor in determining the success of a novel technology. To date, results about degradation of PCCs during long-term experiments are scarce as the technology is nascent. The study conducted by Zhou et al. reported a voltage drift of 40 mV/1000 h during PCCEL at −1.0 A cm^{-2} and 650 °C over a period of 1833 h [28]. In the present study, the short-term stability of PCCEL under variable electrolysis current was investigated first at 550 and 600 °C with 30% H_2O supplied to the positrode (Fig. S8). By increasing the current density from −0.2 to −1.0 A cm^{-2}, the terminal voltage remained stable and constant at each step, demonstrating the stability of the cell at various current densities. Another fresh cell was tested for 1680 h to assess the long-term durability. The corresponding life cycle is shown in Fig. 3(a). In the first 300 h, a mixture of 10% H_2O in air was supplied to the positrode, and the cell was operated at −0.4 A cm^{-2}, corresponding to a cell voltage of 1.180 V. The cell voltage remained constant over the period, suggesting a negligible degradation. At t = 300 h, the current density was set to −0.8 A cm^{-2}, corresponding to a terminal voltage of 1.294 V that is slightly above V_{TN} (1.28 V). The cell was operated in these conditions for 215 h. The power interruption at t = 432 h did not cause any significant damage to the cell, as the nominal operating voltage of ∼1.294 V was recovered, demonstrating the robustness of the tested cell.

At t = 515 h, the steam content in the positrode gas feed was increased to 30%, while the current was kept constant at −0.8 A cm^{-2}. The cell was operated in these conditions until t = 1680 h. By increasing the steam content from 10% to 30%, the terminal voltage dropped by 23 mV from ∼1.294 to ∼1.271 V. The cell voltage was nearly stable or slightly decreasing for several hundred hours until another power supply failure occurred at t = 1251 h. After the power recovery, the voltages turned back to 1.291 V. Although there is still a difference of ∼20 mV, the results confirm the excellent stability of the cell with BGLC1082–BZCY541 and its robustness when operated at −0.8 A cm^{-2}. After this long-term experiment, the cell was investigated by means of SEM (Fig. 3b). No indication of delamination could be detected between the two electrode/electrolyte interfaces. Moreover, the elemental

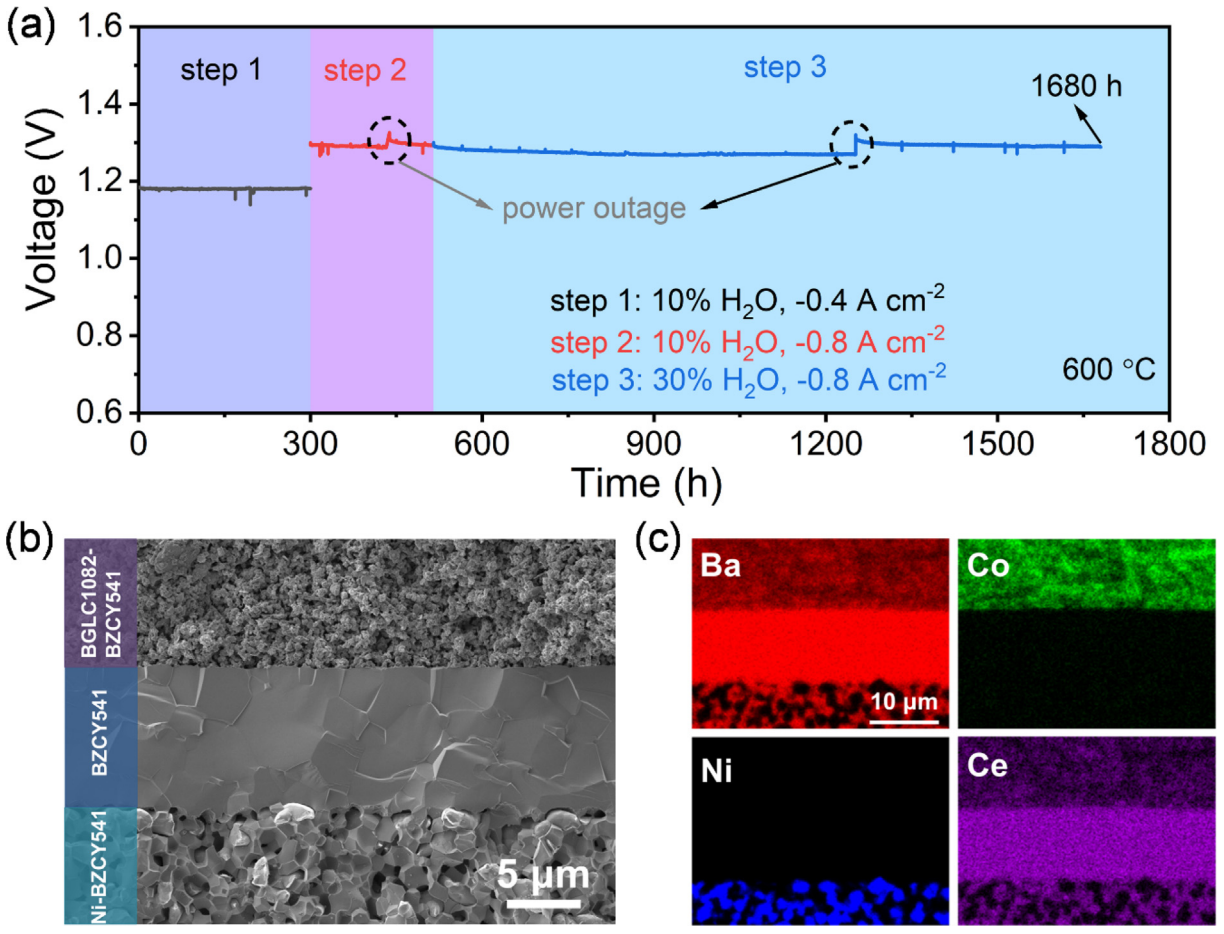

Fig. 3. Long-term stability of PCCs measured in steam electrolysis mode. (a) The voltage evolution in galvanostatic mode with 10%–30% steam/air in the positrode and 20% H_2/N_2 in the negatrode at 600 °C for 1680 h. (b) Cross-section SEM image and (c) EDX elemental mapping of the PCC after long-term steam electrolysis measurement for 1680 h.

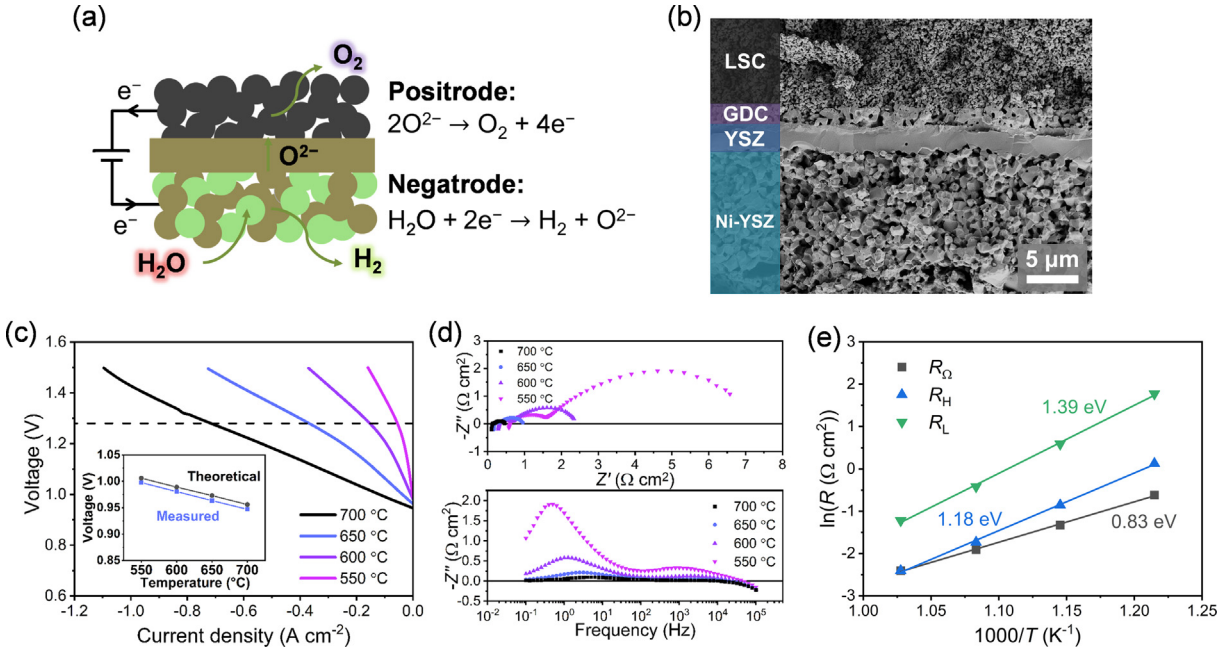

Fig. 4. Characterization of a state-of-the-art commercial SOC for steam electrolysis. Air was supplied to the positrode and a mixture of 20% H_2-30% H_2O-50% N_2 was supplied to the negatrode. (a) Schematic illustration of SOCs for steam electrolysis. (b) SEM cross-section image of the commercial SOC. (c) Polarization curves as a function of current density (inside, the comparison between the measured open circuit voltage and the theoretical value). (d) Nyquist and Bode plots of the electrochemical impedance spectra recorded at OCV. (e) Arrhenius plots of the ohmic resistance (R_Ω) and the polarization resistance (R_H and R_L).

distribution remained homogeneous within the different materials (Fig. 3c, additional elements showing in Fig. S9). It should be noted that Ni migration was not observed at the negatrode after the long time PCCEL operation, despite a current density as high as –0.8 A cm^{-2}. SEM images with higher magnifications in Fig. S10 did not show any evidence of microstructural change in both electrodes, demonstrating the high reliability of the PCC under the tested conditions. This feature is to be compared with the voltage drift of about 40 mV kh^{-1} reported for negatrode supported SOCs operated in steam electrolysis [38], whose Ni-YSZ cermet electrode is prone to degradation. Though its origin is not clearly elucidated, this degradation is possibly related to Ni migration via surface diffusion of $Ni(OH)_x$ species especially at high operating current density and high relative humidity content, leading to the high degradation rate in SOCs [8,9,39]. This suggests that optimization strategies for mitigating degradation in electrolysis are likely to differ between PCCs and SOCs.

3.4. Hydrogen production and energy efficiency at intermediate temperatures

State-of-the-art commercial SOCs (ASC-400B, Elcogen AS, Estonia) were tested for the sake of comparison between SOEL and PCCEL at intermediate temperatures. The same test apparatus and comparable testing conditions to PCCEL were used for SOEL, and the results are shown in Fig. 4. In principle, one of the main differences between SOEL and PCCEL (Fig. 1a) is that in SOEL, the steam is supplied to the SOC negatrode (Fig. 4a). A distinctive feature of the reference SOC is the ~3 μm thin YSZ electrolyte (Fig. 4b), which was developed for intermediate SOEL operation. During electrolysis, the current densities at V_{TN} reach −0.055, −0.153, −0.368 and −0.716 A cm^{-2} at 550, 600, 650 and 700 °C, respectively. The apparent values of the current density obtained in SOEL were lower than those obtained in PCCEL over the entire temperature range. In contrast, the deviation between V_{OC} and V_T in SOEL is limited (less than 1%) compared to PCCEL and does not show any temperature dependence (insert Fig. 4c). The small difference is supposed to be originating from a fraction of gas leakage at the sealing area. Since YSZ electrolyte can be considered as a pure oxygen ion conductor in the tested operating range, the faradaic efficiency of SOEL is considered to be close to 100% [40–42]. Fig. 4(d) shows the EIS recorded at OCV. The R_Ω mainly represents the losses associated to the oxygen ion transport through the electrolyte. R_Ω values in the SOC are 0.54, 0.27, 0.15 and 0.09 Ω cm^2 at 550, 600, 650 and 700 °C, respectively. The corresponding activation energy of 0.83 eV for R_Ω in SOCs agrees with oxygen ion transport (Fig. 4e) [43,44]. In the PCC, the corresponding values of $R_{\Omega,i}$ are 0.38, 0.31, 0.26 and 0.20 Ω cm^2 with an associated activation energy of 0.29 eV for $R_{\Omega,i}$ for the transport of protons (Fig. 1e). The ohmic losses in SOCs were lower than in PCCs at temperatures above 600 °C. While, below this temperature, the ohmic losses in PCCs became lower than in SOCs. The thin electrolyte in the commercial SOCs enable to reduce the ohmic resistance significantly [45]. However, the higher activation energy for oxygen ion conduction compared to proton conduction, makes it challenging to achieve high performance at low temperatures, i.e., below 600 °C with state-of-the-art YSZ electrolyte. The higher proton conductivity values (Fig. S7) in conjunction with a lower activation energy makes PCCs more suited for operation at lower temperatures. By analogy with SOCs, the reduction of electrolyte thickness in PCCs can be a suitable strategy to further improve cell performance at lower temperatures, though its relative impact will be reduced in magnitude due to the lower activation energy value. It is important to note that a reduced electrolyte thickness is likely to increase the current leakage through the PCC electrolyte which may in fine be unfavorable from an energetic point of view. PCCs optimization with thin film electrolyte pose an interesting challenge that deserves further study [46].

The Nyquist plot in Fig. 4(d) suggests 2 depressed arcs; therefore, the EIS spectra recorded on the SOC were fitted by the equivalent circuit with 2 RQ elements (Fig. S4b). The E_a corresponding to high frequency resistances (R_H) and low frequency resistances (R_L) are 1.18 and 1.39 eV, respectively. Again, both values are higher than the characteristic ones in PCCs (Fig. 1e). At low frequency, the main difference may be attributed to the steam diffusion. The diffusion length of steam on positrode side in PCCs is typically ~30 μm (Fig. 1a), whereas it is about 400 μm in the reference SOC negatrode we tested, which is more than an order of magnitude greater. Considering various overpotential losses in the full cells, the losses originating from the gas diffusion make one of the major distinctions between proton conducting and oxygen ion conducting ceramic cells especially at high current density. By using a mathematical analysis, Zheng et al. reported that PCCs possess lower concentration overpotentials compared to SOCs in the negatrode-supported cell configuration [47].

The H_2 production rate in PCCEL was calculated as a function of the terminal voltage at different temperatures (Fig. 5a). The production rates are 1.78, 2.86, 4.39 and 5.30 mL min^{-1} cm^{-2} at 550, 600, 650 and 700 °C and 1.28 V. The H_2 production rates in SOEL were calculated based on the polarization curves upon the reasonable assumption of a 100% faradaic efficiency (Fig. 5b). PCCEL demonstrated a higher H_2 production rate than SOEL at all tested temperatures.

In addition to the hydrogen production rate, the electricity consumption is also a very important factor that determines the price of the produced hydrogen. The electricity consumption was calculated for 1 kg H_2 production at V_{TN} for PCCEL and SOEL by considering the current densities and hydrogen production rate (Fig. 6a–c). In a single cell level analysis, only the electricity supplied to the cells was considered as the power input which can be defined as

$$\text{power(input)} = V \times I, \tag{5}$$

where I is the current and V is the terminal voltage. The energy conversion efficiency can be described as

$$\eta_{ECE} = \frac{\text{power(output)}}{\text{power(input)}}, \tag{6}$$

where the power (output) is the chemical energy of the produced hydrogen. Considering the lower heating value for hydrogen, the power (output) can be written as

$$\text{power(output)} = \frac{I \times \eta_{FE}}{z \times F} \times \Delta H_{H_2,LHV}, \tag{7}$$

where I is the current, η_{FE} is faradaic efficiency, z is 2 for steam electrolysis, F is Faraday's constant and $\Delta H_{H_2,\,LHV}$ is the low heating value for hydrogen (241.8 kJ mol^{-1} or 33.33 kW h kg^{-1}).

At V_{TN} for SOEL, the electricity consumption is ~34 kW h kg^{-1}, which is very close to the lower heating value of hydrogen and remains temperature independent. Thus, η_{ECE} remains close to 100% over the entire temperature range for SOEL (Fig. 6c). However, in PCCEL, the specific electricity consumption was consistently higher and increased from 54 to 66 kW h kg^{-1} upon temperature increase from 550 up to 700 °C at V_{TN} (Fig. 6c). This specific energy consumption is to be compared with other electrolysis technologies at low temperature such as PEMEL (47–66 kW h kg^{-1}), AEL (47–66 kW h kg^{-1}) and AEMEL (51.5–66 kW h kg^{-1}) [48].

In PCCEL, the energy consumption above 33.33 kW h kg^{-1} of produced hydrogen is an energy that must be supplied to the cell without being converted into hydrogen molecules. This additional energy demand is due to the current leakage through the electrolyte, resulting in the lower faradaic efficiency. This corresponds to an energy conversion efficiency η_{ECE} of 62% and 52%, at 550 and

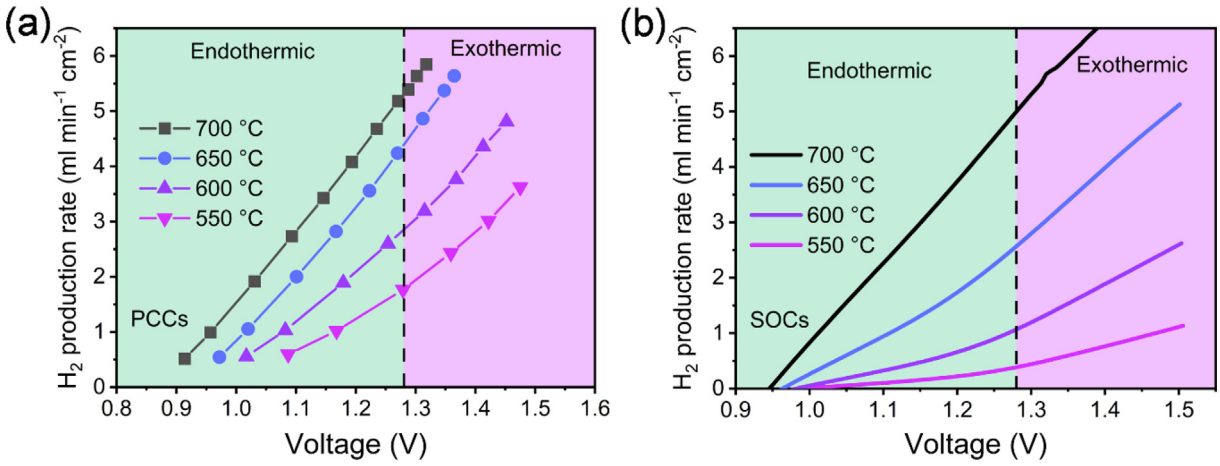

Fig. 5. Hydrogen production rate as a function of voltage at temperatures of 550–700 °C in PCCEL (a) and SOEL (b).

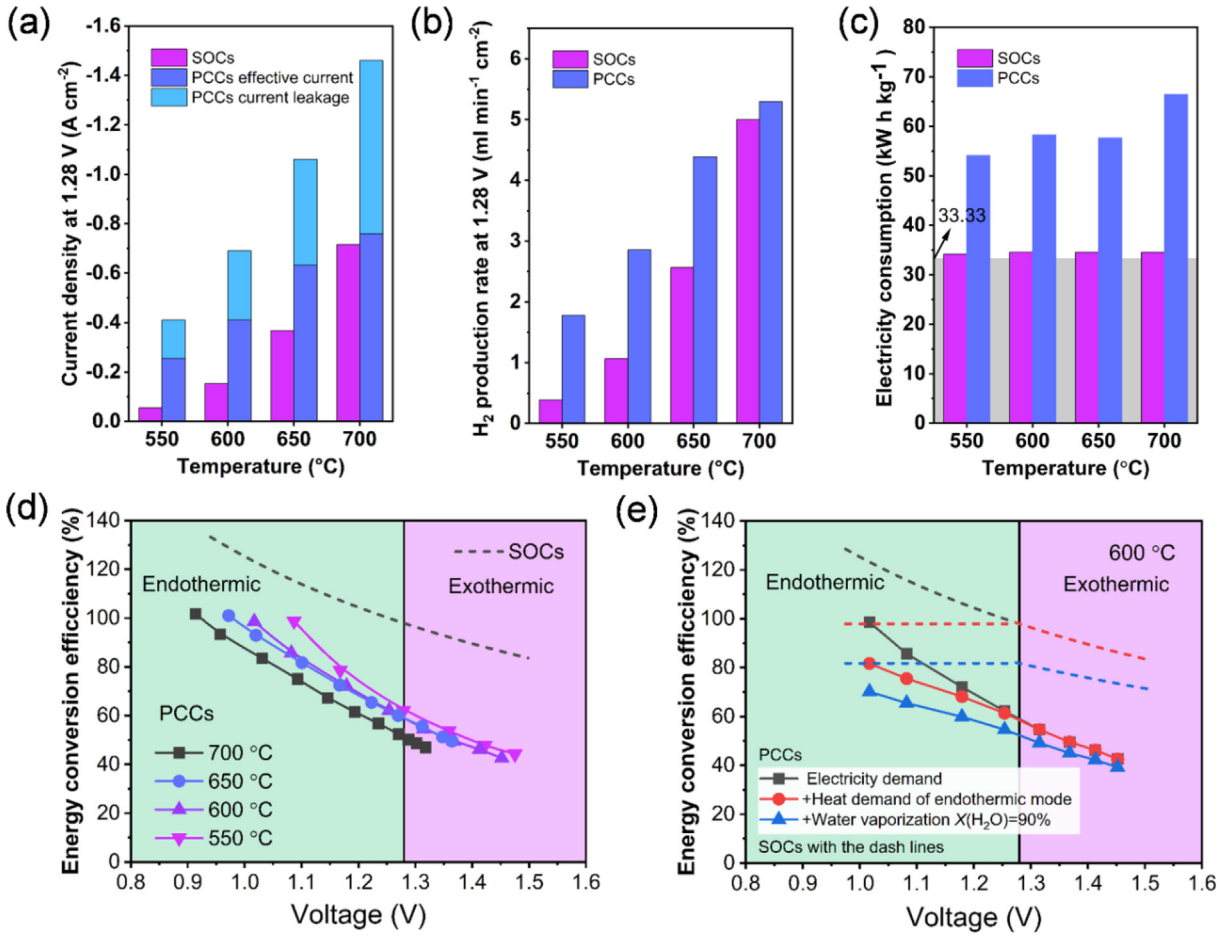

Fig. 6. Comparison between PCCEL and SOEL at thermal neutral voltage (~1.28 V). (a) The current density, (b) hydrogen production rate and (c) electricity consumption for producing 1 kg hydrogen as a function of operating temperatures from 550 to 700 °C. (d) Calculated energy conversion efficiencies of PCCEL and SOEL considering free heat sources. (e) Energy conversion efficiencies of PCCEL and SOEL considering additional heat demand for endothermal operation and water vaporization.

700 °C, respectively (Fig. 6d). Therefore, a lower operating temperature is favorable to reduce current leakage and thus to promote the energy efficiency in PCCEL. Endothermal operation, which is at a terminal voltage below V_{TN}, is an attractive feature of this electrolysis technology, as electrical efficiencies above 100% can be reached at the cell level in SOCs. In endothermal operating regime that is at low overpotential, η_{ECE} for PCCEL ranges from ~60% to ~100% (Fig. 6d). Nonetheless, endothermal operation consumes energy that must be accounted into the energy input unless provided by a free heat source for a more accurate evaluation. This part of energy can be written as

$$\text{power}\,(V_{cell} < V_{TN}) = (V_{TN} - V_{cell}) \times I \times \eta_{FE}\,. \quad (8)$$

Additionally, the vaporization of water is energy consumption as well, and this part of energy can be written as

$$\text{Power(watervaporization)} = \frac{\lambda_{H_2O} \times I \times \eta_{FE}}{z \times F \times X(H_2O)}, \quad (9)$$

where λ_{H_2O} is the water latent heat and $X(H_2O)$ is the water conversion rate. For the calculation, a high conversion rate was assumed to be 90%, which is aligned with industrial values for SOEL. Considering electricity as the energy source for endothermal operation, the η_{ECE} for SOEL decreased down to around 100% (Fig. 6e). The energy demand for water vaporization accounts for additional ~20 points of efficiency. In PCCEL, the energy conversion efficiency remains lower than for SOEL, however with a reduced gap in the endothermal operating zone. At the system level, the gap can be further reduced to the benefit of PCCEL if one considers the necessary purification of hydrogen. Due to the ambipolar transport of oxygen ions and protons in PCC electrolyte, a small steam partial pressure of ~0.3% is established on the negatrode side [24], depending on the oxygen ion transference number. In SOEL, steam content can be as high as 20% in the outlet gas. If water vapor is separated by condensation, there are approximately two orders of magnitude of thermal energy in water vapor that could be wasted in SOEL compared to PCCEL.

In summary, considering the overpotential dependency of the hole concentration and, consequently, the faradaic efficiency (Eq. (4)), PCCEL operated in an endothermal mode appears even more meaningful than for any other electrolysis technology and is to be favored to maximize energy conversion efficiency. This would require an external heat source at sufficient temperature in order to maintain the system at the right operating temperature and avoid cooling. Considering that a temperature of 600 °C is more favorable for the handling of superheated steam than a temperature of 800 °C that would be required for conventional SOEL, this makes PCCEL a technology of choice for the valorization of high temperature waste heat.

4. Conclusions

The BGLC1082-BZCY541 composite positrode for PCCs exhibits high electrocatalytic activity towards ORR and OER at intermediate temperatures (500–700 °C). We demonstrated a PCC cell with excellent durability in electrolysis mode at ~1.28 V for 1680 h with a current density as high as –0.8 A cm^{-2}. This is 8 times higher than the previous report on tubular cells. The electrolysis cell operated at intermediate temperatures with a specific energy consumption comprised between 54 and 66 kW h kg^{-1}, which is comparable to low temperature electrolysis technologies, while showing a hydrogen production rate systematically higher than SOEL performed with a commercial reference cell. In other words, at the rated hydrogen production, PCCEL requires less active surface area than SOEL. The reduced faradaic efficiency and comparatively low energy conversion efficiency in PCCEL are caused by the current leakage through the BZCY electrolyte. This can be mitigated by operation at reduced temperatures and in endothermal mode, which makes PCCEL a technology of choice to valorize high temperature waste heat from industrial processes into hydrogen. To increase the faradaic efficiency, by optimizing materials, the cell design, or the operating strategy is a key challenge to address for future developments of PCCEL in order to achieve even more superior techno-economic merits.

Declaration of competing interest

The authors declare that they have no known competing financial interests or personal relationships that could have appeared to influence the work reported in this paper.

Acknowledgments

The China Scholarship Council is acknowledged for the doctoral scholarship of Haoyu Zheng (201806160173). The German Federal Ministry for Education and Research is acknowledged for funding via the Project ARCADE (03SF0580A).

Appendix A. Supplementary material

Supplementary data to this article can be found online at https://doi.org/10.1016/j.jechem.2023.07.030.

References

[1] IEA, Global Hydrogen Review 2022, https://www.iea.org/reports/global-hydrogen-review-2022, 2022.
[2] M. Younas, S. Shafique, A. Hafeez, F. Javed, F. Rehman, Fuel 316 (2022).
[3] IEA, Hydrogen, https://www.iea.org/reports/hydrogen, 2022.
[4] T. Terlouw, C. Bauer, R. McKenna, M. Mazzotti, Energ. Environ. Sci. 15 (2022) 3583–3602.
[5] W. Zhang, M. Liu, X. Gu, Y. Shi, Z. Deng, N. Cai, Chem. Rev. 123 (2023) 7119–7192.
[6] A. Hauch, S.H. Jensen, S. Ramousse, M. Mogensen, J. Electrochem. Soc. 153 (2006) A1741–A1747.
[7] A. Sciazko, T. Shimura, Y. Komatsu, N. Shikazono, J. Therm. Sci. Technol. 16 (2021) JTST0013.
[8] M.P. Hoerlein, M. Riegraf, R. Costa, G. Schiller, K.A. Friedrich, Electrochim. Acta 276 (2018) 162–175.
[9] M.B. Mogensen, M. Chen, H.L. Frandsen, C. Graves, A. Hauch, P.V. Hendriksen, T. Jacobsen, S.H. Jensen, T.L. Skafte, X. Sun, Fuel Cells 21 (2021) 415–429.
[10] A. Faes, A. Hessler-Wyser, A. Zryd, J. Van Herle, Membranes 2 (2012) 585–664.
[11] L. Bi, S. Boulfrad, E. Traversa, Chem. Soc. Rev. 43 (2014) 8255–8270.
[12] C. Duan, J. Huang, N. Sullivan, R. O'Hayre, Appl. Phys. Rev. 7 (2020).
[13] G.P. Panayiotou, G. Bianchi, G. Georgiou, L. Aresti, M. Argyrou, R. Agathokleous, K.M. Tsamos, S.A. Tassou, G. Florides, S. Kalogirou, P. Christodoulides, Energy Procedia 123 (2017) 335–345.
[14] G. Bianchi, G.P. Panayiotou, L. Aresti, S.A. Kalogirou, G.A. Florides, K. Tsamos, S. A. Tassou, P. Christodoulides, Energy Ecol. 4 (2019) 211–221.
[15] H. An, H.-W. Lee, B.-K. Kim, J.-W. Son, K.J. Yoon, H. Kim, D. Shin, H.-I. Ji, J.-H. Lee, Nat. Energy 3 (2018) 870–875.
[16] C. Duan, J. Tong, M. Shang, S. Nikodemski, M. Sanders, S. Ricote, A. Almansoori, R. O'Hayre, Science 349 (2015) 1321–1326.
[17] C.C. Duan, R. Kee, H.Y. Zhu, N. Sullivan, L.Z. Zhu, L.Z. Bian, D. Jennings, R. O'Hayre, Nat. Energy 4 (2019) 230–240.
[18] D. Han, X. Liu, T.S. Bjørheim, T. Uda, Adv. Energy Mater. 11 (2021) 2003149.
[19] H. Zhu, S. Ricote, C. Duan, R.P. O'Hayre, D.S. Tsvetkov, R.J. Kee, J. Electrochem. Soc. 165 (2018) F581–F588.
[20] H. Zhu, S. Ricote, C. Duan, R.P. O'Hayre, R.J. Kee, J. Electrochem. Soc. 165 (2018) F845–F853.
[21] Y. Zhang, R. Knibbe, J. Sunarso, Y. Zhong, W. Zhou, Z. Shao, Z. Zhu, Adv. Mater. 29 (2017) 1700132.
[22] N. Wang, C. Tang, L. Du, R. Zhu, L. Xing, Z. Song, B. Yuan, L. Zhao, Y. Aoki, S. Ye, Adv. Energy Mater. 12 (2022) 2201882.
[23] R. Strandbakke, V.A. Cherepanov, A.Y. Zuev, D.S. Tsvetkov, C. Argirusis, G. Sourkouni, S. Prunte, T. Norby, Solid State Ion. 278 (2015) 120–132.
[24] E. Vøllestad, R. Strandbakke, M. Tarach, D. Catalan-Martinez, M.L. Fontaine, D. Beeaff, D.R. Clark, J.M. Serra, T. Norby, Nat. Mater. 18 (2019) 752–759.
[25] H. Zheng, M. Riegraf, N. Sata, R. Costa, J. Mater. Chem. A 11 (2023) 10955–10970.
[26] E. Vøllestad, M. Schrade, J. Segalini, R. Strandbakke, T. Norby, J. Mater. Chem. A 5 (2017) 15743–15751.
[27] K. Leonard, J. Druce, V. Thoreton, J.A. Kilner, H. Matsumoto, Solid State Ion. 319 (2018) 218–222.
[28] Y. Zhou, E. Liu, Y. Chen, Y. Liu, L. Zhang, W. Zhang, Z. Luo, N. Kane, B. Zhao, L. Soule, Y. Niu, Y. Ding, H. Ding, D. Ding, M. Liu, ACS Energy Lett. 6 (2021) 1511–1520.
[29] J.H. Kim, S. Yoo, R. Murphy, Y. Chen, Y. Ding, K. Pei, B. Zhao, G. Kim, Y. Choi, M. Liu, Energ. Environ. Sci. 14 (2021) 1506–1516.
[30] Y. Chen, Y. Choi, S. Yoo, Y. Ding, R. Yan, K. Pei, C. Qu, L. Zhang, I. Chang, B. Zhao, Y. Zhang, H. Chen, Y. Chen, C. Yang, B. deGlee, R. Murphy, J. Liu, M. Liu, Joule 2 (2018) 938–949.
[31] M. Liu, H. Hu, J. Electrochem. Soc. 143 (1996) L109–L112.
[32] D. Huan, W. Wang, Y. Xie, N. Shi, Y. Wan, C. Xia, R. Peng, Y. Lu, J. Mater. Chem. A 6 (2018) 18508–18517.
[33] K. Katahira, Y. Kohchi, T. Shimura, H. Iwahara, Solid State Ion. 138 (2000) 91–98.
[34] S. Choi, T.C. Davenport, S.M. Haile, Energ. Environ. Sci. 12 (2019) 206–215.
[35] K.D. Kreuer, Annu. Rev. Mat. Res. 33 (2003) 333–359.
[36] M. Burriel, J. Peña-Martínez, R.J. Chater, S. Fearn, A.V. Berenov, S.J. Skinner, J.A. Kilner, Chem. Mater. 24 (2012) 613–621.

[37] M.V. Ananyev, V.A. Eremin, D.S. Tsvetkov, N.M. Porotnikova, A.S. Farlenkov, A. Y. Zuev, A.V. Fetisov, E.K. Kurumchin, Solid State Ion. 304 (2017) 96–106.
[38] F. Tietz, D. Sebold, A. Brisse, J. Schefold, J. Power Sources 223 (2013) 129–135.
[39] M.B. Mogensen, A. Hauch, X. Sun, M. Chen, Y. Tao, S.D. Ebbesen, K.V. Hansen, P. V. Hendriksen, Fuel Cells 17 (2017) 434–441.
[40] J. Schefold, A. Brisse, F. Tietz, J. Electrochem. Soc. 159 (2011) A137–A144.
[41] J. Schefold, A. Brisse, M. Zahid, ECS Trans. 28 (2010) 357–367.
[42] C.M. Stoots, J.E. O'Brien, K.G. Condie, J.J. Hartvigsen, Int. J. Hydrog. Energy 35 (2010) 4861–4870.
[43] C. Korte, A. Peters, J. Janek, D. Hesse, N. Zakharov, PCCP 10 (2008) 4623–4635.
[44] R. Devanathan, W. Weber, S. Singhal, J. Gale, Solid State Ion. 177 (2006) 1251–1258.
[45] F. Han, R. Mücke, T. Van Gestel, A. Leonide, N.H. Menzler, H.P. Buchkremer, D. Stöver, J. Power Sources 218 (2012) 157–162.
[46] Y. Matsuzaki, Y. Tachikawa, Y. Baba, K. Sato, G. Kojo, H. Matsuo, J. Otomo, H. Matsumoto, S. Taniguchi, K. Sasaki, J. Electrochem. Soc. 167 (2020).
[47] K.-Q. Zheng, M. Ni, Q. Sun, L.-Y. Shen, Acta Mech. Sin. 29 (2013) 388–394.
[48] IRENA (2020), Green Hydrogen Cost Reduction: Scaling up Electrolysers to Meet the 1.5 °C Climate Goal, International Renewable Energy Agency, Abu Dhabi.